PNAS RESEARCH ARTICLE | EARTH, ATMOSPHERIC, AND PLANETARY SCIENCES OPEN ACCESS

Stormier Southern Hemisphere induced by topography and ocean circulation

Tiffany A. Shaw[a,1], Osamu Miyawaki[a], and Aaron Donohoe[b]

Edited by Michael Mann, The Pennsylvania State University, University Park, PA; received December 30, 2021; accepted October 29, 2022

A defining feature of Earth's present-day climate is that the Southern Hemisphere is stormier than the Northern Hemisphere. Consistently, the Southern Hemisphere has a stronger jet stream and more extreme weather events than the Northern Hemisphere. Understanding the relative importance of land–ocean contrast, including topography, radiative processes, and ocean circulation for determining this storminess asymmetry is important and may be helpful for interpreting projections of future storminess. Here, we show that the stormier Southern Hemisphere is induced by nearly equal contributions from topography and the ocean circulation, which moves energy from the Southern to Northern Hemisphere. These findings are based on 1) diagnostic energetic analyses applied to observations and climate model simulations and 2) modifying surface (land and ocean) boundary conditions in climate model simulations. Flattening topography and prescribing hemispherically symmetric surface energy fluxes (the manifestation of ocean energy transport on the atmosphere) in a climate model reduce the storminess asymmetry from 23 to 12% and 11%, respectively. Finally, we use the energetic perspective to interpret storminess trends since the beginning of the satellite era. We show that the Southern Hemisphere has become stormier, consistent with implied ocean energy transport changes in the Southern Ocean. In the Northern Hemisphere, storminess has not changed significantly consistent with oceanic and radiative (increased absorption of sunlight due to the loss of sea ice and snow) changes opposing one another. The trends are qualitatively consistent with climate model projections.

extratropical storms | ocean circulation | climate change

Significance

Storms and extreme weather events are stronger in the Southern Hemisphere than in the Northern Hemisphere. Using an energetic perspective, observations, and climate model simulations, we show that the stormier Southern Hemisphere is induced by topography and the ocean circulation, which transports energy from the Southern to the Northern Hemisphere. We also show that the recent increase in Southern Hemisphere storminess is connected to changes in implied ocean energy transport in the Southern Ocean. Northern Hemisphere storminess has not changed significantly because the ocean changes are opposed by the absorption of sunlight due to the loss of sea ice and snow. These observed changes are qualitatively consistent with climate model projections.

A defining feature of Earth's present-day climate is that extratropical storminess in the Southern Hemisphere is stronger than its Northern Hemisphere counterpart (1–4). The jet stream is also stronger in the Southern Hemisphere (5). These differences are important because they result in more precipitation and wind extremes across the extratropical Southern Hemisphere (6, 7). The relative roles of land–ocean contrast, including topography, radiative processes, and ocean circulation in determining this storminess asymmetry is unknown. Uncovering the mechanisms controlling present-day storminess is an important step toward understanding future projections of storminess, including their societal impacts (4, 8).

Present-day storminess in the Southern Hemisphere is distributed nearly homogeneously across the Southern Ocean (Fig. 1*A*). In contrast, Northern Hemisphere storminess is localized mostly over ocean basins (Fig. 1*B*). The storminess asymmetry (Southern minus Northern Hemisphere) reflects land and ocean boundary conditions in the Northern Hemisphere (Fig. 1*C*). More specifically, the longitudinal regions where the Southern Hemisphere is stormier (orange contours, Fig. 1*C*) coincide with regions of large topography over Eurasia and North America. When averaged over longitude and across the extratropics (poleward of 20° latitude), the Southern Hemisphere is 24% stormier than the Northern Hemisphere across reanalysis data sets (*SI Appendix*, Fig. S1*A*). The storminess asymmetry is largest in the upper troposphere (*SI Appendix*, Fig. S1*B*) and is also clear in the jet stream (*SI Appendix*, Fig. S1*C*).

The observed storminess asymmetry can be simulated in an atmospheric model forced with topography and observationally derived climatological surface energy fluxes (the manifestation of ocean energy transport on the atmosphere, see *Methods*). The model captures both the spatial structure (c.f. Figs. 1*C* and 2*A*) and the extratropical storminess asymmetry, which is 23% in the model compared to 24% in observations (c.f. *SI Appendix*, Fig. S1*A*, Fig. 2*E*, and Table 1, ALL).

Author affiliations: [a]Department of the Geophysical Sciences, The University of Chicago, Chicago, IL 60637; and [b]Applied Physics Laboratory, University of Washington, Seattle, WA 98105

Author contributions: T.A.S. designed research; T.A.S., O.M., and A.D. performed research, analyzed data, and wrote the paper.

The authors declare no competing interest.

This article is a PNAS Direct Submission.

[1]To whom correspondence may be addressed. Email: tas1@uchicago.edu.

This article contains supporting information online at https://www.pnas.org/lookup/suppl/doi:10.1073/pnas.2123512119/-/DCSupplemental.

Published December 5, 2022.

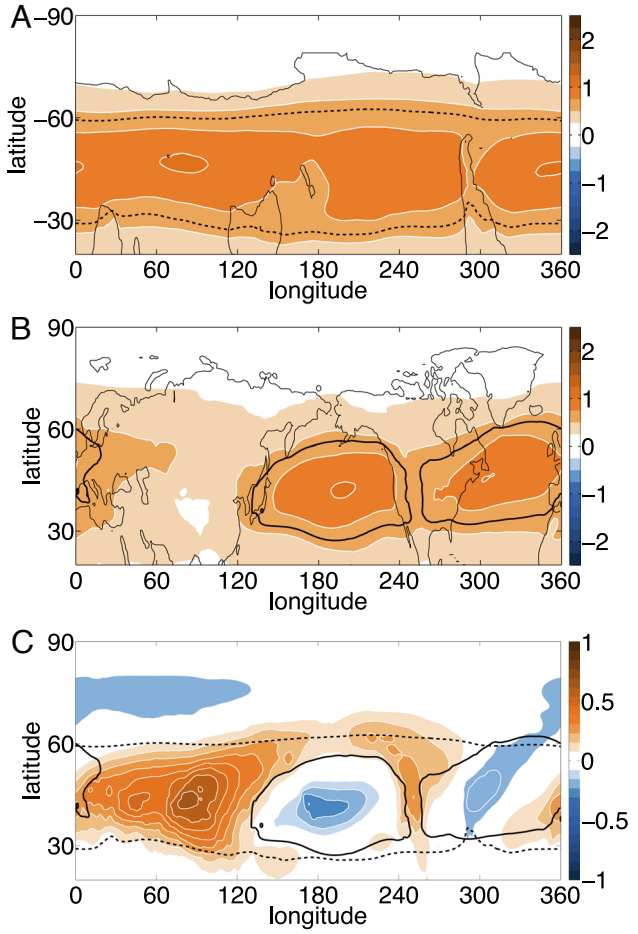

Fig. 1. Observed annual-mean storminess (averaged across reanalysis data sets) as measured by cosine-weighted vertically integrated eddy kinetic energy (MJ m^{-2}) from 1980 to 2018 for the (*A*) Southern Hemisphere, (*B*) Northern Hemisphere, and (*C*) their difference. The black lines indicate where storminess is equal to 0.6 MJ m^{-2} for the Southern (dashed) and Northern (solid) hemispheres.

Topographic Contribution to Present-Day Storminess

Results from early climate model simulations showed that flattening topography increases storminess in the Northern Hemisphere. However, the model did not capture the observed storminess asymmetry (Southern Hemisphere storminess was biased) (9). Here, we show flattening topography in a model, which captures the observed storminess asymmetry and reduces but does not eliminate the asymmetry (Fig. 2*B*). Storminess increases in both hemispheres when the topography is flattened (Table 1, FLAT), but Southern Hemisphere storminess is still stronger than Northern Hemisphere storminess across the Eastern Hemisphere and between 30° and 45° latitude in the Western Hemisphere (Fig. 2*B*). When averaged over longitude and across the extratropics the storminess asymmetry is reduced from 23% to 12% with flattened topography (Fig. 2*E*, FLAT), which is large compared to the end-of-century projections of the response of storminess to anthropogenic climate change (10).

An existing framework based on temperature (10, 11) cannot explain the reduced storminess asymmetry when topography is flattened (see MAPE, Table 1). Instead, we turn to an energetic framework, which connects extratropical storminess (STM) to three factors: the equator-to-pole imbalance of top-of-atmosphere radiative fluxes (TOA), the equator-to-pole imbalance of surface energy flux (SFC), and stationary circulation atmospheric energy flux (SC):

$$STM = TOA - SFC - SC, \quad [1]$$

(*Methods*, (12)). Topography impacts the hemispheric asymmetry of energetic storminess via the stationary circulation atmospheric energy flux (SC term in Eq. **1**) (13, 14).

In observations, the rescaled energetic storminess asymmetry (STM) is 23% and can be diagnostically decomposed into a 12% contribution from surface energy fluxes (−SFC), a 14% contribution from stationary circulation atmospheric energy flux (−SC), and a small −3% contribution from TOA radiative fluxes (*SI Appendix*, Fig. S2). The small TOA contribution is consistent with the small hemispheric asymmetry of TOA radiative fluxes (15–17). When the model is forced with topography and observationally derived climatological surface energy fluxes, it captures the diagnostic decomposition of the energetic storminess asymmetry in observations, namely a 12% contribution from surface energy fluxes (−SFC), a 14% contribution from stationary circulation atmospheric energy flux (−SC), and a small −3% contribution from TOA radiative fluxes (Fig. 2*F*, ALL).

When topography is flattened in the model, the stationary circulation contribution to the storminess asymmetry is negligible (consistent with its connection to topography) and the remaining asymmetry is due to surface energy fluxes (Fig. 2*F*, FLAT). Thus, the model simulation with flattened topography confirms the causal connection between the stationary circulation energy flux (SC in Eq. **1**) and topography. Furthermore, it shows that topography accounts for about half of the storminess asymmetry.

Oceanic Contribution to Present-Day Storminess

Another important source of hemispheric asymmetry is the ocean circulation. The ocean transports energy poleward in both hemispheres but also across the equator from the Southern to the Northern Hemisphere via the ocean overturning circulation (18). The ocean overturning circulation is known to modulate the wintertime climate of the Northern Hemisphere, including the intensity of storminess in the North Atlantic (19–23). Frierson et al. (16) showed that the ocean overturning circulation contributes to the hemispheric asymmetry of tropical precipitation. However, the impact of the ocean circulation on the storminess asymmetry has not been previously examined.

Here, we hypothesize that the ocean makes the present-day Southern Hemisphere stormier than the Northern Hemisphere via the following energetic mechanism. The ocean overturning circulation transports energy from the Southern to the Northern Hemisphere converging energy into the Arctic. The hemispheric asymmetry of ocean energy transport manifests onto the atmospheric energy budget as a hemispheric asymmetry of surface energy fluxes (16) (provided the land and ocean surface is in equilibrium). Thus, due to ocean circulation alone, the Southern Hemisphere should be stormier than the Northern Hemisphere because it leads to a weaker equator-to-pole imbalance of surface energy fluxes in the North. The ocean circulation impacts the hemispheric asymmetry of energetic storminess via the surface energy flux (surface energy fluxes term in Eq. **1**). Note that this mechanism suggests that if the hemispheric asymmetry of surface energy fluxes were eliminated, then the storminess asymmetry would be reduced.

We analyze the impact of the ocean circulation on the storminess asymmetry by forcing the climate model with hemi-

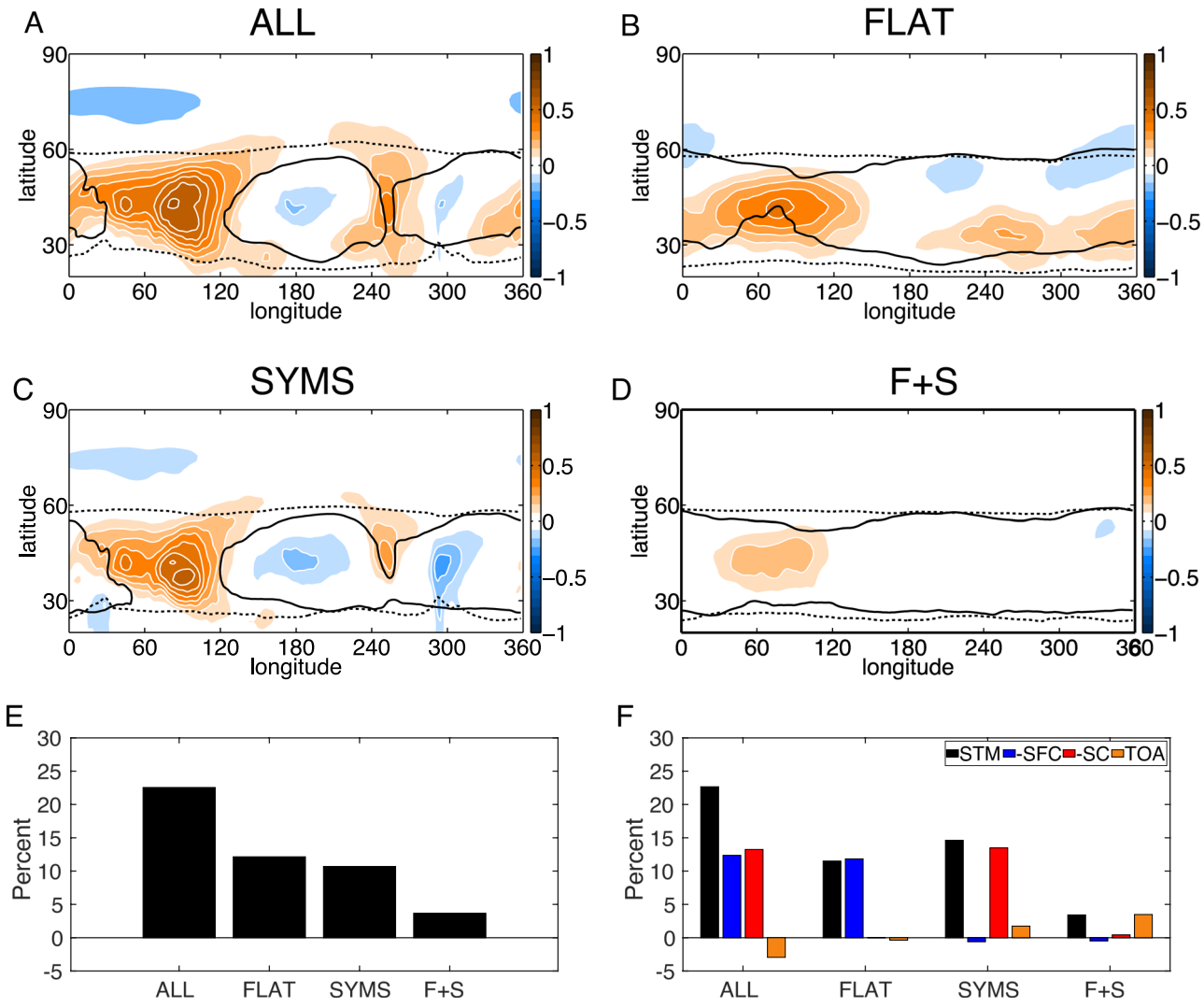

Fig. 2. Difference of Southern and Northern Hemisphere storminess (cosine-weighted vertically integrated eddy kinetic energy, MJ m^{-2}) in the climate model forced with observationally derived climatological surface energy fluxes for (*A*) climatology (ALL), (*B*) flattened topography (FLAT), (*C*) symmetrized surface energy fluxes (SYMS), and (*D*) flattened topography and symmetrized surface energy fluxes (F+S) simulations. The black lines in (*A* and *D*) indicate where storminess is equal to 0.6 MJ m^{-2} for the Southern (dashed) and Northern (solid) hemispheres. Percentage difference of longitudinal-mean, vertically integrated extratropical (poleward of 20°) storminess (difference of Southern and Northern Hemisphere divided by Northern Hemisphere) across the simulations for (*E*) eddy kinetic energy and (*F*) rescaled transient eddy moist static energy flux (STM) decomposed into surface energy flux (SFC), stationary circulation (SC) and top-of-atmosphere (TOA) contributions.

spherically symmetrized surface energy fluxes following (16). Recall that when the climate model is forced with observationally derived climatological surface energy fluxes, it captures the storminess asymmetry (Figs. 2 *A* and *E*, ALL). When the model is forced with hemispherically symmetrized surface energy fluxes, which eliminates the hemispheric asymmetry of ocean energy transport (*SI Appendix*, Fig. S3), the storminess asymmetry decreases (Fig. 2*C*). The decreased asymmetry occurs because Northern Hemisphere storminess increases, whereas Southern Hemisphere storminess decreases (Table 1, SYMS). The impact of symmetrizing surface energy fluxes on storminess is more longitudinally homogeneous than the impact of flattening topography (compare Fig. 2*B* to Fig. 2*C*). However, the storminess asymmetry is still significant over the Eastern Hemisphere and between 45° and 60° latitude in the Western Hemisphere. We interpret this result as the combined impact of topography and land boundary conditions on storminess. When averaged over longitude and across the extratropics, the storminess asymmetry is reduced from 23% to 11% with symmetrized surface energy fluxes (Fig. 2*E*, SYMS).

In order to confirm the role of the ocean circulation, we turn to the energetic framework. When surface energy fluxes are

Table 1. Storminess (vertically integrated eddy kinetic energy, EKE, MJ m^{-2}) and dry (moist) Mean Available Potential Energy (MAPE, MJ m^{-2}) following (10) averaged across the extratropics (poleward of 20°) of the Northern (NH) and Southern (SH) Hemispheres

	EKE_{NH}	EKE_{SH}	$MAPE_{NH}$	$MAPE_{SH}$
ALL	0.81	1.00	2.31 (3.02)	2.96 (3.73)
FLAT	0.95	1.06	2.30 (3.04)	2.90 (3.76)
SYMS	0.83	0.92	2.42 (3.05)	2.81 (3.67)
F + S	0.97	1.00	2.43 (3.08)	2.68 (3.61)

hemispherically symmetrized in the model, the surface energy flux contribution to the storminess asymmetry is negligible (consistent with its connection to the hemispheric asymmetry of implied ocean energy transport) and the remaining asymmetry is due to the stationary circulation energy flux (Fig. 2*F*, SYMS). Thus, the model simulation with hemispherically symmetrized surface energy fluxes shows that the ocean circulation accounts for about half of the storminess asymmetry.

When the model is forced with hemispherically symmetrized surface energy fluxes in the presence of flattened topography, the storminess asymmetry is negligible (Fig. 2*D*), i.e., 3% (Fig. 2*E*, F+S). In particular, Northern Hemisphere storminess is now similar to Southern Hemisphere storminess (Table 1, F+S). The storminess asymmetry in the upper troposphere and the jet stream asymmetry are also negligible (*SI Appendix*, Fig. S4 *A* and *B*). When topography is flattened in the presence of hemispherically symmetrized surface energy fluxes in the model, the stationary circulation and surface energy flux contributions are negligible. The TOA radiative flux contribution leads to a small storminess asymmetry (Fig. 2*F*, F+S).

Thus, the climate model simulations suggest that the stormier Southern Hemisphere is induced by topography and the ocean circulation. Interestingly, the results imply that differences in evaporative resistance over land, land–ocean surface heat capacity, or surface drag do not contribute significantly to the stormier Southern Hemisphere.

Contributions to Strengthening Storminess Asymmetry

Since the beginning of the satellite era, the Southern Hemisphere has become even stormier than the Northern Hemisphere across reanalysis data sets (Fig. 3*A*). This trend reflects a significant strengthening of Southern Hemisphere storminess (P value of the linear coefficient of the linear regression model is <0.05) and no significant change in Northern Hemisphere storminess (*SI Appendix*, Table S1). The multimodel mean storminess asymmetry trends from climate model projections are statistically significant (P value of the linear coefficient of the linear regression model applied to the multimodel mean time series is <0.05 for both CMIP5 and CMIP6) and consistent in sign with reanalysis trends (Fig. 3 *A* and *SI Appendix*, Table S1). However, there is spread across the model ensemble. In particular, the 10th and 90th percentile of the distribution of individual model trends are on either size of zero (see whiskers in Fig. 3*A*). Nevertheless, the multimodel mean of the distribution is statistically significant (P value of the 1-sided t test is <0.05 for both CMIP5 and CMIP6). The recent generation of models (CMIP6) better capture the storminess asymmetry trend but they underestimate the trend in each hemisphere (*SI Appendix*, Table S1).

The energetic perspective can be used to interpret why the Southern Hemisphere is getting stormier. According to the energetic framework, the increasingly stormier Southern Hemisphere (black bar, Fig. 3*B*) is consistent with the trends in surface energy flux (blue bar, Fig. 3*B*) and TOA radiative flux (orange bar, Fig. 3*B*). The surface energy flux trend reflects anomalous equatorward implied ocean energy transport, which is stronger in the Southern Ocean than in the North Atlantic (blue line, *SI Appendix*, Fig. S5*A*). The anomalous implied equatorward transport in the Southern Ocean has been connected to circumpolar upwelling and passive advection by the climatological ocean circulation associated with the transient response to increased CO_2 (24). We note that our analysis cannot distinguish between trends in ocean energy transport and the spatial pattern of ocean energy content, and we use the term "implied" to refer to both processes.

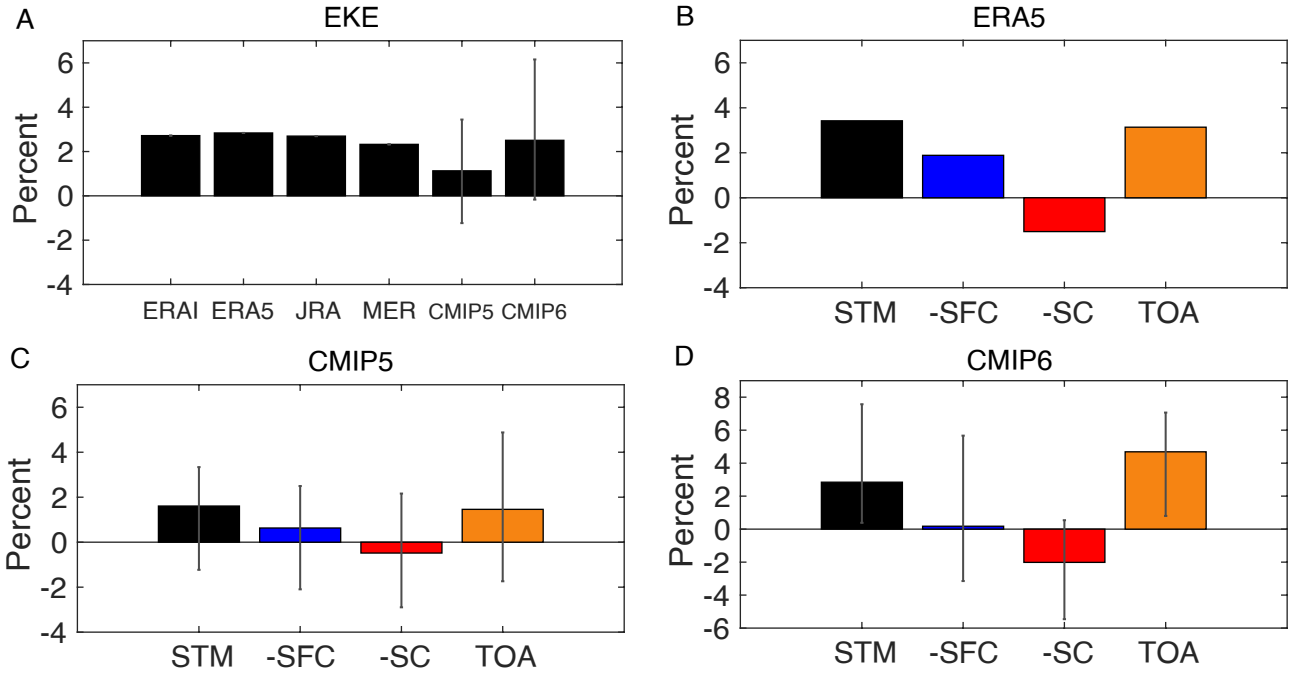

Fig. 3. Trend of storminess asymmetry (difference of Southern and Northern Hemisphere divided by Northern Hemisphere climatology) from 1980 to 2018 for reanalysis data and the Coupled Model Intercomparison Project (CMIP) multimodel mean as measured by vertically integrated (*A*) eddy kinetic energy. Trend of energetic storminess defined by eddy moist static energy flux (STM) decomposed into surface energy flux (SFC), stationary circulation energy flux (SC), and TOA radiative flux (TOA) contributions for (*B*) ERA5 and the (*C*) CMIP5 and (*D*) CMIP6 multimodel mean. All trends are multiplied by 39 y. Whiskers show the 10th and 90th percentile values across the model ensemble.

The hemispheric asymmetry of the TOA radiative flux trend (orange bar, Fig. 3*B*) reflects increased absorption of sunlight in the Northern Hemisphere which is unmatched in the Southern Hemisphere (*SI Appendix*, Fig. S6). Arctic sea ice loss (25) and snow melt over the Northern Hemisphere continents (26, 27) are consistent with enhanced absorption of shortwave radiation in the NH extratropics, which weakens the TOA contribution to Northern Hemisphere storminess (orange line, *SI Appendix*, Fig. S5A) and, thus, results in a positive storminess asymmetry trend (orange bar, Fig. 3B). The hemispheric asymmetry of TOA radiative flux trend is consistent with the transient climate response to increased CO_2, which differs between the hemispheres. In climate models, the transient response to increased CO_2 involves Arctic Sea ice loss, Arctic amplification of surface temperature, snow melt over Northern Hemisphere continents, and land warming more than ocean (28, 29). In contrast, the transient response involves negligible changes in Antarctic Sea ice and no Antarctic amplification of surface temperature. Instead, transient cooling occurs over the Southern Ocean.

The TOA radiative and surface energy flux trends are opposed by the stationary circulation energy flux trend (red bar, Fig. 3*B*). The stationary circulation trend reflects an increase in the Southern Hemisphere stationary circulation energy flux from 20 to 40°S and small changes in the Northern Hemisphere (red line, *SI Appendix*, Fig. S5*A*). The Southern Hemisphere stationary circulation trend is dominated by the mean meridional circulation (Hadley and Ferrel cell) contribution (*SI Appendix*, Fig. S7). The connection between documented trends in the Hadley cell (30, 31) and the stationary circulation energy flux is currently unclear. Our diagnostic analysis also cannot rule out the possibility that the stationary circulation energy flux trend is related to the surface energy flux trend.

The multimodel mean energetic trends from climate model projections are consistent in sign with reanalysis trends (Fig. 3 *C* and *D*). However, there is a significant spread across the model ensemble (see whiskers in Fig. 3 *C* and *D*). The models also do not fully capture the spatial structure of the reanalysis trends (*SI Appendix*, Fig. S5 *B* and *C*).

Discussion

Our results show that the stormier Southern Hemisphere is induced by topography and ocean circulation. We showed that the impact of topography and the ocean circulation could be interpreted using an energetic framework that linked topography to the stationary circulation atmospheric energy flux and the ocean circulation to surface energy fluxes. More specifically, the ocean circulation contributes to a stormier Southern Hemisphere by transporting energy from the Southern to the Northern Hemisphere thereby creating a larger equator-to-pole surface energy flux imbalance in the Southern Hemisphere. The causal impact of topography and ocean circulation was confirmed by combining 1) diagnostic energetic analysis of observations and climate model simulations and 2) climate model simulations with modified (land and ocean) surface boundary conditions (flattened topography and hemispherically symmetrized surface energy fluxes). Interestingly, the results suggest that land–ocean contrast (surface heat capacity, evaporative resistance over land, and surface drag) alone does not result in a stormier Southern Hemisphere.

The energetic perspective of storminess was used to interpret why the Southern Hemisphere has become stormier since the beginning of the satellite era. In particular, the stormier Southern Hemisphere is consistent with anomalous equatorward implied ocean energy transport in the Southern Ocean. In the Northern Hemisphere, TOA radiative changes associated with the loss of sea ice and snow oppose the strengthening of storminess implied by ocean changes. These observed trends are qualitatively consistent with climate model projections of the transient climate response to increased CO_2. Namely, the Southern Hemisphere is projected to become stormier, whereas Northern Hemisphere storminess changes are muted due to a tug of war between tropical and polar climate changes (4, 32).

Our energetic mechanism accounts for thermodynamic coupling between the atmosphere and ocean. It does not preclude the impact of dynamic coupling. Indeed, dynamic coupling between the atmosphere and ocean could contribute to the storminess asymmetry if it significantly impacts surface energy fluxes. A recent study (33) showed that flattening topography in coupled models leads to a weaker ocean circulation, but the impact on storminess is consistent with our atmospheric model results (storminess asymmetry is still significant with flattened topography). The impact of ocean–atmosphere interactions on storminess should be studied further using coupled climate models and observations.

The energetic mechanism linking the ocean circulation to the extratropical storminess asymmetry has implications for our understanding of storminess in past climates. In particular, during the Last Glacial Maximum (LGM), the ocean overturning circulation was weaker than that in present day, which would tend to weaken the storminess asymmetry following the energetic mechanism (weaker Southern Hemisphere storminess). However, the topography was elevated in the Northern Hemisphere during the LGM because of the Laurentide ice sheet, which would tend to strengthen the storminess asymmetry (weaker Northern Hemisphere storminess). There is evidence for weaker North Atlantic storminess (34–36) and small changes in Southern Hemisphere storminess across an ensemble of LGM climate model simulations (37). The energetic framework can be used to futher investigate the connections between radiative fluxes, ocean circulation, topography, and storminess across different climates.

Materials and Methods

Observational Data Products. We use 6 h data provided by ERA-Interim, ERA5, JRA-55, and MERRA2 from 1980 to 2018. We quantify storminess using the vertically integrated transient eddy kinetic energy and eddy moist static energy flux. In both cases, transient eddies are defined as deviations from a monthly average, that is an average over a particular month not the climatological monthly average (12).

Since surface energy fluxes are not measured directly, we create an observational estimate following previous work (16, 38–40). In particular, we estimate the climatological surface energy flux by subtracting atmospheric energy flux divergence estimates based on reanalysis data from satellite observations of TOA radiative flux. The Clouds and the Earth's Radiant Energy System (CERES), Energy Balanced and Filled (EBAF) satellite product data from 2001 to 2018 are used to estimate the TOA radiative flux, and the atmospheric energy flux divergence is estimated using ERA-Interim from 2001 to 2018. While we use the most accurate method for estimating surface energy fluxes, there remains some uncertainty in any energy budget estimate.

Trends in the storminess asymmetry are significant from 1980 to 2018 but not from the 2001 to 2018 period for which satellite-derived TOA radiative fluxes from CERES EBAF is available. In order to understand the storminess trends from 1980 to 2018 and their connection to surface energy fluxes, we use the same method to quantify trends of surface energy fluxes. Namely, we take the difference of TOA radiative flux and atmospheric energy flux divergence and storage (accounting for the small atmospheric energy storage). However, we do not trust trends in the surface energy fluxes from the reanalysis output (i.e., the combination of surface radiative and turbulent energy fluxes in the reanalysis)

due to well-documented unrealistic energy imbalances and drifts (41, 42). Thus, we estimate surface energy fluxes from 1980 to 2018 from the difference of ERA5 TOA radiative flux and the atmospheric energy flux divergence derived from 6 h ERA5 reanalysis data. We use the ERA5 TOA radiative flux data because it agrees better with CERES data from 2001 to 2018 as compared to the other reanalysis TOA radiative fluxes (*SI Appendix*, Fig. S8). In all cases, trends are calculated using a linear regression model. The vertically integrated eddy kinetic energy trends are consistent with the 700 hPa eddy heat flux trends in the Southern Hemisphere (43).

Climate Model Simulations. We simulate storminess using the ECHAM6 slab-ocean atmosphere general circulation model (44). The model has a realistic land surface with topography, a 50 m mixed layer depth, and is forced with the monthly varying climatological surface energy fluxes derived from 1) an observational estimate (see above) following (16) and 2) a q-flux from a prescribed sea surface temperature (AMIP) simulation from 1980 to 2018.

Topography is flattened in the ECHAM6 simulations by setting the surface geopotential and mean orography to zero in the surface boundary condition input file. Symmetrized surface energy fluxes are created following the procedure of ref. 16. Namely, the symmetrized surface energy flux is longitudinally symmetric, with values chosen at each latitude such that the longitudinal integral of the surface energy flux over the ocean is equal to the average between the Northern Hemisphere and Southern Hemisphere longitudinal integrals. The storminess simulated using symmetrized surface energy fluxes and flattened topography are robust to using either the observationally or q-flux-derived surface energy fluxes (compare Fig. 2 to *SI Appendix*, Fig. S9).

We use daily data from 22 coupled CMIP5 models (*SI Appendix*, Table S2) and 18 coupled CMIP6 models (*SI Appendix*, Table S3) to calculate storminess from 1980 to 2018 (historical and RCP8.5/SSP5-8.5). The significant improvement in the mean location of the westerly jet in CMIP6 models (45, 46) does not seem to have improved the storminess trend in the SH as compared to CMIP5 (see *SI Appendix*, Table S1).

Energetic Framework. The moist static energy (MSE) framework for storm track intensity connects extratropical storminess to TOA radiative fluxes, surface energy fluxes, and stationary circulation energy flux via the MSE budget

$$\nabla \cdot F_{TE} = \nabla \cdot F_{TOA} - \nabla \cdot F_{SFC} - \nabla \cdot F_{SC}, \qquad [2]$$

where $F_{TE} = \langle [\overline{v'm'}] \rangle$ and $F_{SC} = \langle [\bar{v}\,\bar{m}] \rangle$ are the MSE flux by transient eddies and stationary circulation (mean meridional circulation plus stationary eddies), respectively, $\nabla \cdot F_{TOA} = R_{TOA}$ and $\nabla \cdot F_{SFC} = S$ are in flux form, where R_{TOA} and S are the TOA radiative and surface energy fluxes with the global mean removed, $\langle \cdot \rangle$ denotes a mass-weighted vertical integration, $[\cdot]$ denotes a zonal average, $\bar{\cdot}$ denotes a monthly average, i.e., an average over a particular month not the climatological monthly average, and $'$ denotes a deviation from the monthly average (12). The removal of the global mean emphasizes latitudinal gradients (15, 47).

An equation for extratropical storminess in each hemisphere is obtained by integrating Eq. **2** between 20° and the pole:

$$\underbrace{\widehat{F_{TE}}}_{STM} = \underbrace{\widehat{F_{TOA}}}_{TOA} - \underbrace{\widehat{F_{SFC}}}_{SFC} - \underbrace{\widehat{F_{SC}}}_{SC}, \qquad [3]$$

where $\widehat{(\cdot)} = \int_{90°}^{20°} 2\pi \cos\phi (\cdot) d\phi$. For the climatology, the SC contribution to the storminess asymmetry is dominated by stationary eddies. The energetic storminess asymmetry is defined as

$$(-\widehat{F_{TE,SH}} - \widehat{F_{TE,NH}})/\widehat{F_{TE,NH}}, \qquad [4]$$

to account for southward energy flux in the Southern Hemisphere. The MSE budget of the hemispheric asymmetry in ECHAM6 is closed to within 5%. More specifically, the hemispheric asymmetry of atmospheric energy flux calculated using TOA radiative and surface energy fluxes differs from the hemispheric asymmetry of atmospheric energy flux calculated using the 6 h wind and MSE data by 5%. For the observations, the surface energy fluxes term is inferred as a residual (see above) for the CMIP5 and CMIP6 simulations. The SC term is inferred as a residual because the coarse vertical pressure grid makes the computation of SC inaccurate.

Energetic storminess is significantly correlated with eddy kinetic energy across the model simulations and reanalysis data ($R^2 = 0.98$, *SI Appendix*, Fig. S10) consistent with previous work (12, 48–50). The latent energy flux contribution accounts for energetic storminess being larger in SYMS than FLAT in Fig. 2*F* even though eddy kinetic energy is larger in FLAT than SYMS (*SI Appendix*, Fig. S11). Note that the larger latent energy flux in SYMS does not affect our overall conclusion that topography and ocean circulation contribute roughly equally to the storminess asymmetry because the role of each can only be attributed to within the nonlinearity, which is 3% (Fig. 2*E*, F+S), or the accuracy of closing of the MSE budget, which is 5%.

In order to quantitatively compare the hemispheric asymmetry of eddy kinetic energy to the hemispheric asymmetry of energetic storminess, we apply a rescaling factor of 0.65, which comes from rescaling the climatology in each hemisphere ($\widehat{EKE_{SH}}/\widehat{F_{TE,SH}} = -0.29$ and $\widehat{EKE_{NH}}/\widehat{F_{TE,NH}} = 0.33$) and follows previous work (49, 50). Note that a rescaling approach is also used to compare eddy kinetic energy to mean available potential energy (11).

Data, Materials, and Software Availability. Data supporting this study are available through Knowledge@UChicago (10.6082/uchicago.3694).

ACKNOWLEDGMENTS. T.A.S., O.M., and A.D. acknowledge the support from NSF (AGS-1742944, AGS-2033467, and AGS-2019647).

1. Y. Guo, E. K. M. Chang, S. S. Leroy, How strong are the Southern Hemisphere storm tracks? *Geophys. Res. Lett.* **36** (2009). L22806, 10.1029/2009GL040733.
2. B. J. Hoskins, K. I. Hodges, New perspectives on the Northern Hemisphere winter storm tracks. *J. Atmos. Sci.* **59**, 1041–1061 (2002).
3. B. J. Hoskins, K. I. Hodges, A new perspective on Southern Hemisphere storm tracks. *J. Clim.* **18**, 4108–4129 (2005).
4. T. A. Shaw *et al.*, Storm track processes and the opposing influences of climate change. *Nat. Geosc.* **9**, 656–664 (2016). 10.1038/NGEO2783.
5. D. L. Hartmann, *Global Physical Climatology* (Elsevier, 2016), p. 453.
6. S. Pfahl, H. Wernli, Quantifying the relevance of cyclones for precipitation extremes. *J. Clim.* **25**, 6770–6780 (2012).
7. M. Messmer, I. Simmonds, Global analysis of cyclone-induced compound precipitation and wind extreme events. *Weather Clim. Extrem.* **32**, 100324 (2021). 10.1016/j.wace.2021.100324.
8. S. Bony *et al.*, Clouds, circulation and climate sensitivity. *Nat. Geosc.* **8**, 261–268 (2015). 10.1038/NGEO2398.
9. S. Manabe, T. B. Terpstra, The effect of mountains on the general circulation of the atmosphere as identified by numerical experiments. *J. Atmos. Sci.* **31**, 3–42 (1974).
10. P. A. O'Gorman, Understanding the varied response of the extratropical storm tracks to climate change. *Proc. Natl. Acad. Sci. U.S.A.* **107**, 19176–19180 (2010). 10.1073/pnas.1011547107.
11. P. A. O'Gorman, T. Schneider, Energy of midlatitude transient eddies in idealized simulations of changed climates. *J. Clim.* **21**, 5797–5806 (2008).
12. T. A. Shaw, P. Barpanda, A. Donohoe, A moist static energy framework for zonal-mean storm-track intensity. *J. Atmos. Sci.* **75**, 1979–1994 (2018).
13. H. Wang, M. Ting, Seasonal cycle of the climatological stationary waves in the NCEP-NCAR reanalysis. *J. Atmos. Sci.* **56**, 3892–3919 (1999).
14. I. M. Held, M. Ting, H. Wang, Northern winter stationary waves: Theory and modeling. *J. Clim.* **15**, 2125–2144 (2002).
15. A. Donohoe, D. S. Battisti, What determines meridional heat transport in climate models? *J. Clim.* **25**, 3832–3850 (2012).
16. D. M. W. Frierson *et al.*, Contribution of ocean overturning circulation to tropical rainfall peak in the Northern Hemisphere. *Nat. Geos.* **6**, 940–944 (2013). 10.1038/NGEO1987.
17. G. L. Stephens *et al.*, The curious nature of the hemispheric symmetry of the Earth's water and energy balances. *Curr. Clim. Change Rep.* **2**, 135–147 (2016).
18. G. K. Vallis, *Climate and the Oceans* (Princeton University Press, 2012), p. 231.
19. R. Seager *et al.*, Is the gulf stream responsible for Europe's mild winters? *Quart. J. Roy. Soc.* **128**, 2563–2586 (2002).
20. D. J. Brayshaw, T. Woollings, M. Velllinga, Tropical and extratropical responses of the North Atlantic atmospheric circulation to a sustained weakening of the MOC. *J. Clim.* **22**, 3146–3155 (2009).
21. C. Wilson, B. Sinha, R. G. Williams, The effect of ocean dynamics and orography on atmospheric storm tracks. *J. Clim.* **22**, 3689–3702 (2009).
22. Y. Kaspi, T. Schneider, Winter cold of eastern continental boundaries induced by warm ocean waters. *Nature* **471**, 621–624 (2011). 10.1038/nature09924.

23. T. Woollings, J. M. Gregory, J. G. Pinto, M. Reyers, D. J. Brayshaw, Response of the North Atlantic storm track to climate change shaped by ocean-atmosphere coupling. *Nat. Geos.* **5**, 313–317 (2012). 10.1038/NGEO1438.
24. K. C. Armour, J. Marshall, J. R. Scott, A. Donohoe, E. R. Newsom, Southern Ocean warming delayed by circumpolar upwelling and equatorward transport. *Nat. Geosc.* **9**, 549–554 (2016). 10.1038/NGEO2731.
25. D. L. Hartmann, P. Ceppi, Trends in the CERES dataset, 2000–13: The effects of sea ice and jet shifts and comparison to climate models. *J. Clim.* **27**, 2444–2456 (2014).
26. C. Derksen, R. Brown, Spring snow cover extent reductions in the 2008–2012 period exceeding climate model projections. *Geophys. Res. Lett.* **39**, L19504 (2012). 10.1029/2012GL053387.
27. H. A. Hernández-Henréquez, S. J. Déry, C. Derksen, Polar amplification and elevation-dependence in trends of northern hemisphere snow cover extent, 1971–2014. *Environ. Res. Lett.* **10**, 044010 (2015). 10.1088/1748-9326/10/4/044010.
28. R. J. Stouffer, S. Manabe, K. Bryan, Interhemispheric asymmetry in climate response to a gradual increase of atmospheric CO_2. *Nature* **342**, 660–662 (1989).
29. S. Manabe, R. J. Stouffer, M. J. Spelman, K. Bryan, Transient responses of a coupled ocean-atmosphere model to gradual changes of atmospheric CO_2. Part I: Annual mean response *J. Clim.* **4**, 785–818 (1991).
30. C. M. Mitas, A. Clement, A recent behavior of the Hadley cell and tropical thermodynamics in climate models and reanalyses. *Geophys. Res. Lett.* **33**, L01810 (2006).
31. R. Chemke, L. M. Polvani, Opposite tropical circulation trends in climate models and in reanalyses. *Nat. Geosc.* **17**, 528–532 (2019). 10.1038/s41561-019-0383-x.
32. E. A. Barnes, J. A. Screen, The impact of Arctic warming on the midlatitude jet-stream: Can it? Has it? Will it? *WIREs Clim. Change* **6**, 277–286 (2015). 10.1002/wcc.337.
33. R. J. Stouffer *et al.*, The role of continental topography in the present-day ocean's mean climate. *J. Clim.* **35**, 1327–1346 (2022). 10.1175/JCLID-20-0690.1.
34. N. M. J. Hall, B. Dong, P. J. Valdes, Atmospheric equilibrium, instability and energy transport at the Last Glacial Maximum. *Clim. Dyn.* **12**, 497–511 (1996).
35. C. Li, D. S. Battisti, Reduced Atlantic storminess during Last Glacial Maximum: Evidence from a coupled climate model. *J. Clim.* **21**, 3561–3579 (2008).
36. A. Donohoe, D. S. Battisti, Causes of reduced North Atlantic storm activity in a CAM3 simulation of the Last Glacial Maximum: Theory and modeling. *J. Clim.* **22**, 4793–4808 (2009).
37. A. Donohoe, K. C. Armour, G. S. Roe, D. S. Battisti, The partitioning of atmospheric energy transport and changes under climate forcing in coupled climate models. *J. Clim.* **33**, 4141–4165 (2020).
38. A. Donohoe, D. S. Battisti, The seasonal cycle of atmospheric heating and temperature. *J. Clim.* **26**, 4962–4980 (2013).
39. K. E. Trenberth, J. T. Fasullo, An observational estimate of ocean energy divergence. *J. Phys. Ocean.* **38**, 985–999 (2008).
40. C. Liu *et al.*, Evaluation of satellite and reanalysis-based global net surface energy flux and uncertainty estimates. *J. Geophys. Res.* **122**, 6250–6272 (2017). 10.1002/2017JD026616.
41. M. Wild *et al.*, The global energy balance from a surface perspective. *Clim. Dyn.* **40**, 3107–3134 (2013).
42. M. Wild *et al.*, The energy balance over land and oceans: An assessment based on direct observations and CMIP5 climate models. *Clim. Dyn.* **44**, 3393–3429 (2015).
43. R. Chemke, L. M. Polvani, Linking midlatitudes eddy heat flux trends and polar amplification. *NPJ Climate and Atmos. Sci.* **3**, 8 (2020). 10.1038/s41612-020-0111-7.
44. B. Stevens *et al.*, Atmospheric component of the MPI-M Earth System Model: ECHAM6. *J. Adv. Model. Earth Syst.* **5**, 146–172 (2013).
45. T. J. Bracegirdle *et al.*, Improvements in circumpolar southern hemisphere extratropical atmospheric circulation in CMIP6 compared to CMIP5. *Earth Space Sci.* **7**, e2019EA00106 (2020). 10.1029/2019EA001065.
46. R. Goyal, A. S. Gupta, M. Jucker, M. England, Historical and projected changes in the southern hemisphere surface westerlies. *Geophys. Res. Lett.* **48**, e2020GL090849 (2021). 10.1029/2020GL090849.
47. S. M. Kang, I. M. Held, D. M. W. Frierson, M. Zhao, The response of the ITCZ to extratropical thermal forcing: Idealized slab-ocean experiments with a GCM. *J. Clim.* **21**, 3521–3532 (2008).
48. P. Barpanda, T. A. Shaw, Surface fluxes modulate the seasonality of zonal-mean storm tracks. *J. Atmos. Sci.* **77**, 753–779 (2020).
49. T. A. Shaw, R. J. Graham, Hydrological cycle changes explain weak Snowball Earth storm track despite increased surface baroclinicity. *Geophys. Res. Lett.* **47**, e2020GL08986 (2020). 10.1029/2020GL089866.
50. T. A. Shaw, Z. Smith, The midlatitude response to polar sea ice loss: Idealized slab-ocean aquaplanet experiments with thermodynamic sea ice. *J. Clim.* **35**, 2633–2649 (2022).